



HAL
open science

Tetragonal tungsten bronze phase thin films in the K–Na–Nb–O system: Pulsed laser deposition, structural and dielectric characterizations

Barthélemy Aspe, Valérie Demange, Anne Waroquet, Xavier Castel, Brice Gautier, Quentin Simon, David Albertini, Mustapha Zaghrioui, Kevin Nadaud, S. Députier, et al.

► To cite this version:

Barthélemy Aspe, Valérie Demange, Anne Waroquet, Xavier Castel, Brice Gautier, et al.. Tetragonal tungsten bronze phase thin films in the K–Na–Nb–O system: Pulsed laser deposition, structural and dielectric characterizations. *Journal of Alloys and Compounds*, 2020, 827, pp.154341. 10.1016/j.jallcom.2020.154341 . hal-02482183

HAL Id: hal-02482183

<https://hal.science/hal-02482183v1>

Submitted on 2 Apr 2020

HAL is a multi-disciplinary open access archive for the deposit and dissemination of scientific research documents, whether they are published or not. The documents may come from teaching and research institutions in France or abroad, or from public or private research centers.

L'archive ouverte pluridisciplinaire **HAL**, est destinée au dépôt et à la diffusion de documents scientifiques de niveau recherche, publiés ou non, émanant des établissements d'enseignement et de recherche français ou étrangers, des laboratoires publics ou privés.

Credit Authors Statement

B. Aspe: Conceptualization, Formal Analysis, Investigation, Writing – Original draft, Visualization

V. Demange: Conceptualization, Formal Analysis, Investigation, Supervision, Writing – Original Draft, Visualization, funding acquisition

A. Waroquet: Investigation, Resources

X. Castel: Conceptualization, Formal Analysis, Investigation, Supervision, Writing, Visualization, funding acquisition

B. Gautier: Conceptualization, Formal Analysis, Investigation, Writing, Visualization

Q. Simon: Conceptualization, Formal Analysis, Investigation, Writing, Visualization

D. Albertini: Formal Analysis, Investigation, Resources

M. Zaghrioui: Conceptualization, Formal Analysis, Investigation, Writing, Visualization

K. Nadaud: Conceptualization, Formal Analysis, Investigation, Writing, Visualization

S. Députier: Conceptualization, Investigation, Resources, Writing

F. Gouttefangeas: Formal Analysis, Investigation, Resources

R. Sauleau: Conceptualization, Formal Analysis, Investigation, Supervision, Writing, Visualization, funding acquisition

M. Guilloux-Viry: Conceptualization, Investigation, Supervision, Writing, Project Administration, funding acquisition

Tetragonal tungsten bronze phase thin films in the K-Na-Nb-O system: pulsed laser deposition, structural and dielectric characterizations

B. Aspe^{a,b}, V. Demange^{a,c}, A. Waroquet^a, X. Castel^b, B. Gautier^d, Q. Simon^e, D. Albertini^d, M. Zaghrioui^e, K. Nadaud^e, S. Députier^a, F. Gouttefangeas^c, R. Sauleau^b, M. Guilloux-Viry^{a,c}

^a Univ Rennes, CNRS, ISCR – UMR 6226, F-35000 Rennes, France

^b Univ Rennes, CNRS, IETR – UMR 6164, F-35000 Rennes, France

^c Univ Rennes, CNRS, ScanMAT – UMS 2001 F-35000 Rennes, France

^d Univ Lyon, CNRS, UMR 5270, Inst Nanotechnol Lyon, Inst Natl Sci Appl Lyon, F-69621 Villeurbanne, France

^e GREMAN – UMR 7347, University of Tours, CNRS, INSA CVL, F-41000 Blois, France

Corresponding authors:

Maryline Guilloux-Viry: email address: maryline.guilloux-viry@univ-rennes1.fr
ORCID identifier: 0000-0001-7773-1643
phone number: +33 (0) 2 23 23 56 55

Valérie Demange: email address: valerie.demange@univ-rennes1.fr
ORCID identifier: 0000-0002-8153-2660
phone number: +33 (0) 2 23 23 67 88

Barthélemy Aspe: email address: barthelemy.aspe@univ-rennes1.fr
ORCID identifier: 0000-0001-8927-4013
phone number: +33 (0) 2 23 23 65 70

The authors have no conflict of interest in this work.

ABSTRACT

Pulsed laser deposition parameters have been determined to synthesize pure Tetragonal Tungsten Bronze (TTB) phase thin films in the (K,Na)-Nb-O system (KNN). In relation to the high volatility of alkaline elements, it was found that the target composition and the target-substrate distance are of first importance. The TTB phase was identified by X-ray and electron diffraction and the surface microstructure consisting mainly of nanorods supports the formation of hallmark of the TTB phase. Poly-oriented nanorods have been obtained on both C-plane sapphire and (111)Pt/TiO₂/SiO₂/(001)Si substrates whereas horizontal nanorods oriented along the (*hk*0) planes have been grown on (100) and (110) SrTiO₃. All the nanorods are parallel together when grown on (110) SrTiO₃ and they present two in-plane orientations rotated of 90° from each other on (100) SrTiO₃. Dielectric characteristics (dielectric permittivity ϵ_r , and loss tangent $\tan\delta$) have been measured at low (1 kHz - 1 MHz) and high (1 GHz - 40 GHz) frequencies, on films deposited on Pt coated silicon and sapphire, respectively. A value of $\epsilon_r = 200$ at 1 kHz with $\tan\delta = 0.015$ were measured in a parallel plate capacitor configuration, whereas $\epsilon_r = 130$ and $\tan\delta = 0.20$ at 10 GHz were retrieved from transmission lines printed on the KNN TTB thin film grown on C-plane sapphire. Raman investigations of the TTB films were performed in the temperature range 77 - 873 K, confirming the TTB phase formation and the absence of structural transition. Piezoelectric Force Microscopy measurements evidenced a piezoelectric signal although no switching could be performed. However the dielectric measurements, complicated by high leakage currents when a DC voltage was applied, did not evidence any proof of ferroelectricity for the undoped KNN TTB films whereas results reported on other niobates (A,A')_{0.6}Nb₁₀O₃₀ (with A: K, Na and A': Sr, Ba, Ca) have shown Curie temperatures, lying between 156°C and

560°C, separating the paraelectric phase (space group: $P4/mbm$ N°127) and the ferroelectric one (space group: $P4bm$ N°100).

1. INTRODUCTION

Ferroelectric and piezoelectric materials have a wide range of applications from sensors to micro-electro-mechanical systems (MEMS), memory devices and tunable devices, e.g. [1–3]. For decades, the $\text{PbZr}_{1-x}\text{Ti}_x\text{O}_3$ -based (PZT) material has been the most popular ferroelectric materials [4]. Lately an effort has been made by the scientific community to find a more ecologic and less toxic alternative to this material. Since 2004, the $\text{K}_x\text{Na}_{1-x}\text{NbO}_3$ perovskite-type material has been established to be a potential substitute for PZT due to its high piezoelectric coefficient d_{33} (up to 300 pC/N [5]) leading to an important investigation of this phase [6, 7]. The $\text{K}_x\text{Na}_{1-x}\text{NbO}_3$ perovskite phase has been investigated in bulk [8], thin films [9], single crystals [10] and for photovoltaic applications [11], energy storage [12], luminescence properties [13], sensors [14] or medical imaging [15]. However, in the KNN system, many other phases of potential interest exist without being thoroughly investigated. In many chemical systems, such as K-Nb-O (KN), K-Ta-O, K-Li-Nb-O (KLN) or K-Ta-Nb-O, chemically close to the KNN system, Tetragonal Tungsten Bronze (TTB) phases have been reported either as thin films or bulk [16–20]. The TTB structure can be described along the [001] direction by two cationic octahedral sites B1 and B2 and three cationic tunnels A1, A2 and C, as presented in Figure 1. A1 and A2 sites can be occupied by alkaline metals, alkaline earth, rare-earth and a few other elements. B1 and B2 sites can mostly be occupied by small and highly charged cations, such as Nb^{5+} , Ta^{5+} or W^{6+} . Finally, the C sites can only be occupied by small cations and are often found to be empty.

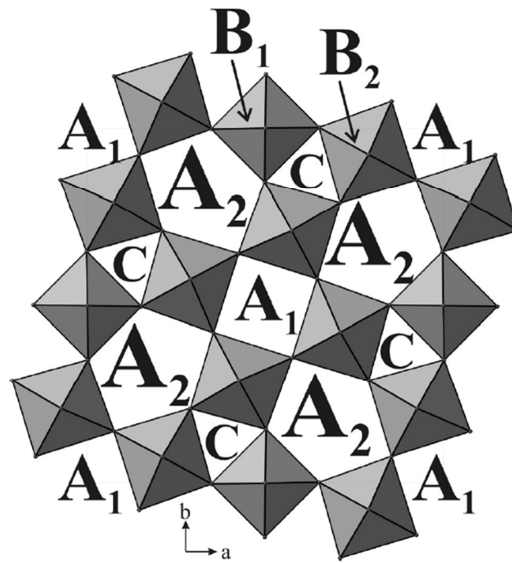


Figure 1. Projection of the tetragonal tungsten bronze structure along the [001] direction showing the three cationic tunnels A1, A2, and C, and the cationic octahedral sites B1 and B2 [16].

Over the years this crystallographic structure with different cationic sites [21] which authorizes many cationic substitutions and doping possibilities was found to be of interest for exhibiting various properties. For example, in the KLN system, a TTB single crystal study has reported values of piezoelectric coefficient d_{33} equal to 52 pC/N and ferroelectric polarization P_r of 25-30 $\mu\text{C}/\text{cm}^2$ [22]. Piezoelectric coefficients d_{33} were measured reaching 190 pC/N and 114 pC/N, for MnO_2 -doped and K-doped TTB ceramics in the Sr-Ca-Na-Nb-O system, respectively [23, 24]. In the Sr-Ba-Na-Nb-O system, the TTB phase exhibits a relative permittivity as high as 1600 at 1 kHz [25]. This structure is also studied for optical properties [26] and catalytic activities [27]. In the KNN system, even though the TTB phase has been found as a secondary phase in bulk perovskite [28–30], the pure phase was neither reported nor properly characterized. Some previous works on a modified $\text{K}_x\text{Na}_{1-x}\text{NbO}_3$ perovskite ceramic have reported that the TTB phase, as a secondary phase, could explain the increase of the piezoelectric properties [29]. The presence of this secondary phase is related to an alkaline deficiency in the ceramic product. Indeed, the $(\text{K},\text{Na})_6\text{Nb}_{10}\text{O}_{30}$ TTB phase is 40 % lower in alkaline elements than the $(\text{K},\text{Na})\text{NbO}_3$ perovskite phase.

As no precise description of the KNN system exists when the alkaline/niobium ratio is less than 1, an analogy with the KN system, chemically close to the KNN system has to be made to obtain the TTB phase. In such a system however, various phases are shown to exist with different alkaline/niobium ratios making the pure TTB phase hard to obtain. Nonetheless, the pulsed laser deposition (PLD) technique is suitable for this type of investigation. Indeed, if the method is known to be congruent in the absence of volatile cation, it offers also a great possibility to tune the composition of the films, either by the modification of the target one and/or by the modification of the deposition parameters. Therefore because of the high alkaline (especially potassium) volatility, a thorough investigation of the deposition parameters is requested to grow the pure phase [31].

In this work, KNN thin films were grown by pulsed laser deposition to control pure TTB phase. The films were deposited on different substrates, *i.e.* single crystals (100) and (110) SrTiO₃, C-plane sapphire and (111)Pt/TiO₂/SiO₂/(001)Si. SrTiO₃ was used here to control the orientation while C-plane sapphire and (111)Pt/TiO₂/SiO₂/(001)Si were used to provide suitable samples for physical measurements. A particular attention was paid to the influence of the deposition parameters on the composition and the structure of the films.

The morphology, structural features and composition have been first investigated using scanning electron microscopy (SEM), X-ray diffraction (XRD), transmission electron microscopy (TEM), Raman spectroscopy and energy-dispersive X-ray spectroscopy (EDXS) analyses. In addition, dielectric properties (relative permittivity and intrinsic loss tangent) have been measured at low (from 1 kHz to 1 MHz) and high (from 1 GHz to 40 GHz) frequencies.

2. EXPERIMENTAL SECTION

2.1. Elaboration of the KNN targets

The ceramic targets were prepared from KNN powders synthesized by solid state reaction at 940°C for 4 hours in air, from sodium carbonate Na_2CO_3 (RP NORMAPUR 99.8%), anhydrous potassium carbonate K_2CO_3 (ACROS Organics 99%) and niobium oxide Nb_2O_5 (Alfa Aesar 99.5%) powders preliminary mixed in a planetary ball-mill and then calcined. Afterwards 25-mm in diameter targets were sintered either by conventional sintering at 1000°C for 12 h in air, or by Spark Plasma Sintering (SPS, FCT System GmbH). Indeed in the case of the deposition of the perovskite films, KNO_3 enriched targets are used in order to obtain the final alkaline/niobium ratio of 1. Because of its low melting point, the addition of KNO_3 in the target favors its sintering [32]. This is not the case for the deposition of TTB thin films which is performed through a non-enriched target. As the target density impacts the overall quality of the thin films and the droplet formation during deposition [33], the alternative SPS method has been used to enhance target density in comparison with targets obtained by conventional sintering. In that case, the powders are placed into a graphite mold which maintains the proper diameter. Graphite foils are introduced between the powder and the mold to facilitate the outmolding. By SPS, a one-step reactive sintering for 10 minutes at 1000°C and about 1 hour of cooling under a 1 bar argon atmosphere leads to a 25-mm-diameter dense KNN ceramic target of which the composition is given in Table 1. A cleaning process of the target of 5 hours at 900°C in air is required to remove the carbon film from the target surface. This step is also used for oxygenation of the ceramic targets. These parameters have been adapted from the work of M. Bah *et al.* [34] and preparation details of each target are summarized in Table 1.

Table 1. Chemical composition and sintering details of the different prepared targets. The accuracy of the composition values is 5 %.

Target number	Targeted composition	Measured composition by SEM EDXS	Sintering technique
---------------	----------------------	----------------------------------	---------------------

Target T1	$(\text{K}_{0.5}\text{Na}_{0.5})\text{NbO}_3$	$(\text{K}_{0.55}\text{Na}_{0.45})_{0.93}\text{NbO}_x$	Standard solid-state sintering at 1000°C for 12 h
Target T2	$(\text{K}_{0.5}\text{Na}_{0.5})_{0.7}\text{NbO}_3$	$(\text{K}_{0.51}\text{Na}_{0.49})_{0.68}\text{NbO}_x$	Standard solid-state sintering at 1000°C for 12 h
Target T3	$(\text{K}_{0.5}\text{Na}_{0.5})_{0.7}\text{NbO}_3$	$(\text{K}_{0.49}\text{Na}_{0.51})_{0.54}\text{NbO}_x$	Spark plasma sintering at 1000°C for 10 minutes

2.2. Elaboration of the KNN thin films by PLD

Thin films were deposited by PLD technique with a KrF excimer laser (Coherent company, pulse duration 20 ns, $\lambda = 248$ nm) sets at a fluence of 2-3 J cm⁻², an energy of 210 mJ and currently at 2 or 4 Hz working frequency. Thin films have been deposited under 0.3 mbar oxygen pressure, at a deposition temperature in the range 600 – 650°C, with a target – substrate distance from 55 to 65 mm. In these conditions the deposition rate is close to 15 nm/min (at 2 Hz) and 30 nm/min (at 4 Hz). In this study the thickness of the films is typically between 250 and 500 nm.

2.3. Choice of the substrates

The films were grown on single crystals (100) and (110) SrTiO₃, C-plane sapphire (i.e. (0001) Al₂O₃) and (111)Pt/TiO₂/SiO₂/(001)Si from Crystal GmbH supplier. SrTiO₃ (perovskite structure with a dielectric permittivity ϵ_r higher than 300) is a model substrate for the growth of oxides in view to control their orientation. Sapphire is suitable for high frequency applications thanks to its low dielectric permittivity and loss values ($\epsilon_r \approx 10$ and $\tan\delta \approx 10^{-4}$ at 10 GHz and room temperature). For the fabrication of the microwave devices, the films have been deposited on 10 mm × 10 mm × 0.5 mm C-plane sapphire substrates. Finally Pt coated silicon (5 mm × 10 mm × 0.7 mm) is well adapted for dielectric measurements in parallel plate capacitor geometry. Each substrate was cleaned in acetone and isopropanol, prior to the deposition step.

2.4. Thin films characterizations

The structural characteristics were investigated by X-ray diffraction (XRD) by using a θ - 2θ diffractometer (D8 Advance, BRUKER) with a monochromatized $Cu K_{\alpha 1}$ wavelength ($\lambda = 1.54056 \text{ \AA}$). The surface morphology was observed by scanning electron microscopy (SEM, JSM 7100F, JEOL and MIRA3 Tescan) coupled with an energy dispersive X-ray spectroscopy detector (SEM-EDXS, SDD X-Max 50 mm², Oxford Instruments) to determine the thin film composition. A 5 nm-thick carbon layer was deposited before SEM-EDXS analysis to ensure optimal element detection and especially the potassium one that we have observed to be highly sensitive to charge accumulation effect.

Transmission electron microscopy (TEM) experiments were performed by using a LaB6 JEOL 2100 instrument equipped with an Oxford Aztec 80 mm² SDD device for EDXS analysis (TEM-EDXS). Samples were prepared by scratching the thin film from the substrate with a diamond tip and by collecting the so-obtained particles on an amorphous carbon copper grid (Agar). Bright field and dark field transmission electron micrographs, and electron diffraction patterns were recorded using a GATAN Orius 200D CCD (charge coupled device) camera. Schemes of structures were drawn with CrystalMaker software from CIF files of phases under consideration. Simulations of electron diffraction patterns were obtained with the help of CrystalDiffract extension of CrystalMaker.

Raman measurements *versus* temperature (from 77 to 873 K) were performed on TTB-type KNN coated (111)Pt/TiO₂/SiO₂/(001)Si substrates using Renishaw Invia spectrometer and temperature controller (Linkam THMS 600). A green line (514 nm) of Argon-ion laser was taken as the excitation source with a power lower than 1 mW to hedge again heating effect. The scattered light was collected by a $\times 50$ objective and dispersed by 2400 lines/mm grating in the back-scattering configuration.

Piezoelectric Force Microscopy (PFM) images were obtained with a NTEGRA NT-MDT system using the so-called « Dual Frequency Resonant Tracking » mode, which enables to

enhance the signal to noise ratio by working near the contact resonance frequency of the tip-sample system. Platinum-Iridium tips have been used, with stiffness in the 2-10 N.m⁻¹ range. In amplitude images, bright zones correspond to higher amplitudes of vibration.

The low frequency dielectric measurements were performed on parallel plate capacitors. Top Au electrodes of surface area S ($\varnothing = 300 \mu\text{m}$, thickness $t_{\text{Au}} = 200 \text{ nm}$) were deposited by magnetron sputtering technique through shadow mask on KNN coated (111)Pt/TiO₂/SiO₂/(001)Si substrates. The capacitance C and the loss tangent ($\tan\delta$) were measured at room temperature from 1 kHz to 1 MHz with an AC driving voltage $V_{\text{ac}} = 125 \text{ mV}$, using an Agilent 4294A impedancemeter. The dielectric permittivity ϵ_r of each sample was retrieved from the measured capacitance (C) using the parallel plate capacitor formula, where t_{KNN} is the thickness of the KNN film:

$$\epsilon_r = \frac{C \times t_{\text{KNN}}}{\epsilon_0 \times S} \quad (1)$$

2.5. Microwave devices for dielectric characterization at microwave frequencies

The dielectric characteristics and frequency tunability of the KNN TTB thin films were investigated using coplanar waveguide (CPW) and transmission lines devices designed with a 3-D commercial electromagnetic software (Ansys HFSSTM). Three 50- Ω lines (8 mm, 5 mm and 3 mm long) with a conductor width $w_l = 40 \mu\text{m}$ surrounded by a gap $g_l = 50 \mu\text{m}$ (Figure 2) were implemented to retrieve the thin films dielectric characteristics (ϵ_r , $\tan\delta$), from the microwave measurements. A CPW quarter-wavelength open-ended stub resonator was also designed to operate in X-band. Its resonance frequency F_r depends upon the stub length L_r and the effective permittivity ϵ_{eff} of the heterostructure, as follows:

$$F_r = \frac{c}{4L_r \sqrt{\epsilon_{\text{eff}}}} \quad (2)$$

where c is the speed of light in vacuum. The devices were fabricated from a 2 μm -thick silver overlayer grown on a 5 nm-thick titanium underlayer deposited by RF magnetron sputtering at room temperature. The silver thickness is three times larger than the skin depth value ($\delta = 0.64 \mu\text{m}$) at 10 GHz. Note that the ultrathin titanium film is used here only to ensure the strong adhesion of the silver film onto the ferroelectric oxide. Standard photolithography and wet etching processes were implemented to pattern the devices. Gold wire bondings (15 μm -diameter and 250 μm -length) were used to enforce the equipotential condition on both CPW grounds and prevent from the excitation of parasitic slotline mode (Figure 2).

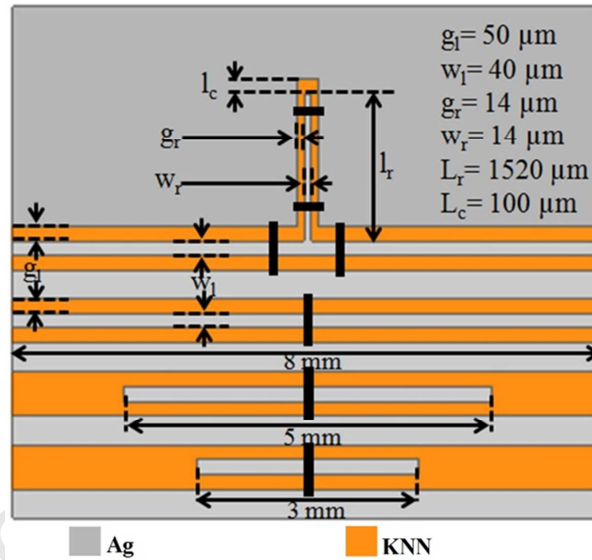


Figure 2. Layout and dimensions of the CPW devices.

Microwave measurements at room temperature and from 20°C to 240°C were carried out through a probe station coupled to a vector network analyzer (VectorSTAR MS4644B, ANRITSU) from 1 to 40 GHz under an external DC bias voltage range from 0 to 150 V, which corresponds to a maximal static electric field E_{bias} equal to 90 kV/cm for the stub resonator and 27 kV/cm for the transmission lines. The measured gap dimensions ($g_r \approx 16 \mu\text{m}$ and $g_l \approx 52 \mu\text{m}$) are slightly larger than the nominal ones due to the inherent overetching of the used wet etching process. Further details are reported elsewhere [35].

3. RESULTS AND DISCUSSION

3.1. Influence of the deposition parameters to grow pure KNN TTB thin films on the various substrates

From a previous study [32] it has been shown that among the various deposition parameters, the target composition, the deposition temperature and the target – substrate distance D have a strong impact on the thin films composition and crystallization, explaining their accurate assessment impact. Table 2 gathers the deposition parameters of the films considered in the present study. Since a film thickness of about 250 nm was obtained with the laser frequency of 2 Hz, the frequency was increased to 4 Hz to achieve a thickness near 500 nm, more suitable for the high frequency reconfigurable devices [47].

The samples labelled in Table 2 are the most significant in view to control the TTB single phase in the KNN system.

Table 2. Summary of deposition parameters and different characteristics of the thin films. The accuracy of the composition values is 5 %.

Thin film	Substrate	Target	Freq. (Hz)	Temp. (°C)	Dist. target-sub. (mm)	Identified phase by XRD	Measured composition (EDXS)
F1	(110)SrTiO ₃	T1	2	600	55	Perovskite	TEM (K _{0.4} Na _{0.6}) _{0.92} NbO _x
F2	Nb:(110)SrTiO ₃	T1	2	650	55	Perovskite	TEM (K _{0.14} Na _{0.86}) _{0.79} NbO _x
F3	Nb:(110)SrTiO ₃	T2	2	600	55	TTB + K ₄ Nb ₆ O ₁₇	TEM (K _{0.58} Na _{0.42}) _{0.62} NbO _x
F4	(110)SrTiO ₃	T3	4	650	65	TTB	SEM (K _{0.45} Na _{0.55}) _{0.44} NbO _x
F5	(001)SrTiO ₃	T3	4	650	65	TTB	SEM (K _{0.47} Na _{0.53}) _{0.43} NbO _x
F6	(111)Pt/TiO ₂ /SiO ₂ /(001)Si	T3	4	650	60	TTB + KNb ₃ O ₈	SEM (K _{0.49} Na _{0.51}) _{0.46} NbO _x
F7	C-plane sapphire	T3	4	650	65	TTB	SEM (K _{0.49} Na _{0.51}) _{0.41} NbO _x
F8	C-plane sapphire	T3	4	650	60	TTB	SEM (K _{0.49} Na _{0.51}) _{0.40} NbO _x
F9	C-plane sapphire	T3	4	650	55	TTB + KNb ₃ O ₈	SEM (K _{0.50} Na _{0.50}) _{0.45} NbO _x

First the role of the target composition has been investigated. Since data have not been yet reported on the TTB phase in the KNN system, the knowledge about the KN system [31] chemically close to the KNN one, has been therefore considered. With the aim to obtain a thin film composition close to $(K_xNa_{1-x})_6Nb_{10}O_{30}$ and while taking into account the alkaline elements volatility during the PLD process [31, 32], the $K_{0.5}Na_{0.5}NbO_3$ target (T1) has been first used. As shown in Figure 3a, XRD pattern of the F1 film, grown on (110)SrTiO₃ at 600°C, displays the $K_{0.4}Na_{0.6}NbO_3$ perovskite phase peaks with a (101) preferential growth, in agreement with the Joint Committee on Powder Diffraction Standards (JCPDS) file #00-061-0310 (space group: *Pm* (6); $a = 3.99628 \text{ \AA}$, $b = 3.93776 \text{ \AA}$, $c = 3.99335 \text{ \AA}$, $\beta = 90.3398^\circ$). The SEM micrograph (Figure 3b) shows a F1 film made of crystallites with rectangular shape of about $300 \text{ nm} \times 100 \text{ nm}$, aligned in the plane along the $\langle 100 \rangle$ axis of the substrate. A few crystals (white contrast) with higher size are also observed. The composition determined by SEM-EDXS $(K_{0.4}Na_{0.6})_{0.92}NbO_3$ is in good agreement with the XRD results and the expected depletion in alkaline elements, especially potassium, during the PLD process. Nevertheless, this depletion is not sufficient to achieve the composition range of the TTB phase.

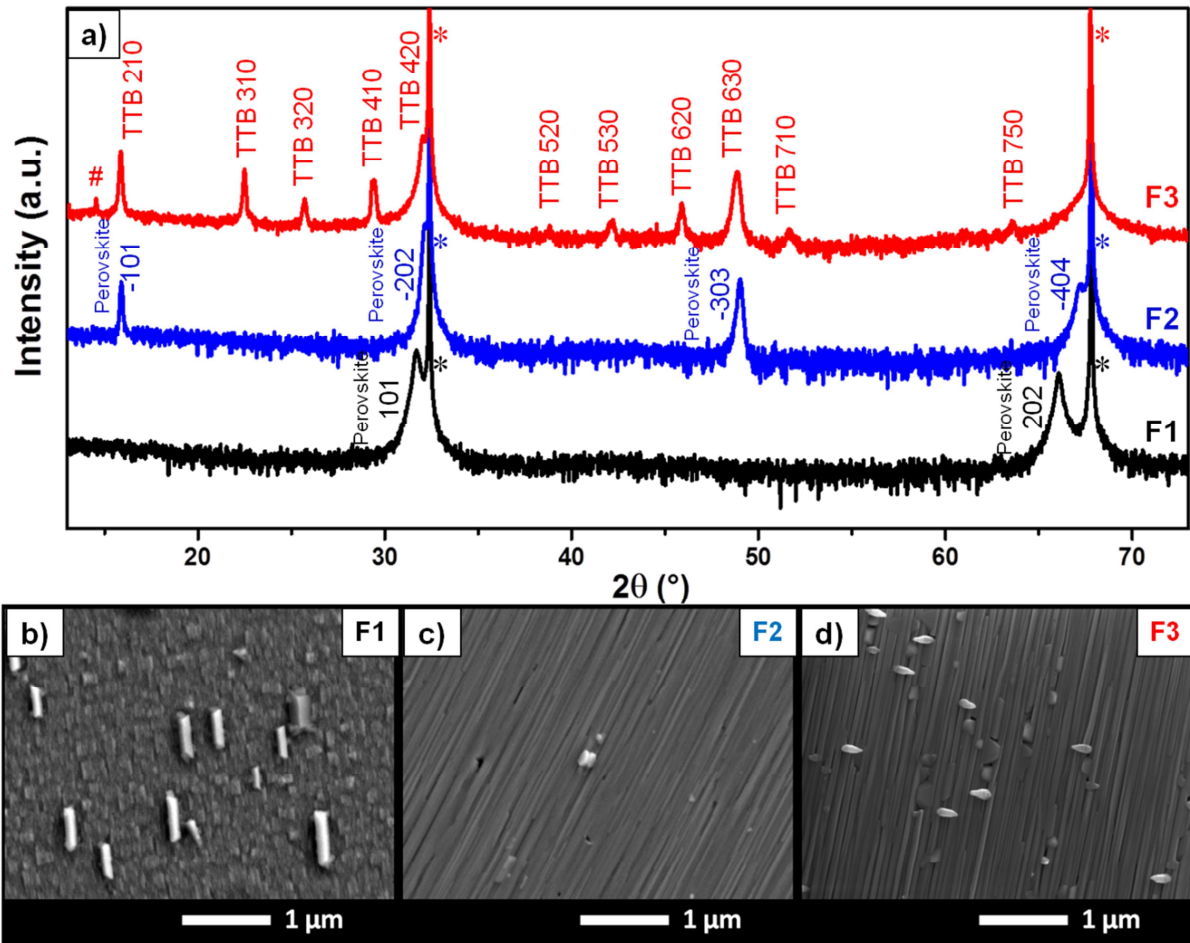


Figure 3. XRD patterns of F1, F2, F3 films (#: $K_4Nb_6O_{17}$ phase, *: substrate) (a). Scanning electron micrographs of F1, F2 and F3 films (b-d).

A second film, namely F2, was grown on the Nb:(110)SrTiO₃ from the same target at higher temperature. The related composition is $(K_{0.14}Na_{0.86})_{0.79}NbO_x$ with a lower amount of alkaline elements, but still too high for the expected composition. The depletion in potassium is particularly high in this sample. Among the several perovskite phases known in this part of the $K_xNa_{1-x}NbO_3$ solid solution, only $K_{0.1}Na_{0.9}NbO_3$ (JCPDS files # 01-074-2025, space group: Pm (6); $a = 7.8720 \text{ \AA}$, 7.7920 \AA , 7.8632 \AA , $\beta = 90.479^\circ$) fits with the XRD pattern, with a $(\bar{1}01)$ preferential growth (Figure 3a). The SEM micrograph shows a film made of very long (several microns) and thin parallel crystallites (50-100 nm wide)(Figure 3c).

To favor the growth of the TTB phase, the alkaline target composition was further decreased down to $(\text{K}_{0.5}\text{Na}_{0.5})_{0.7}\text{NbO}_3$ (target T2). The film obtained at 600°C using this target (F3) leads to the formation of the TTB phase on Nb:(110)SrTiO₃ as displayed by XRD (Figure 3a). On this pattern, only {hk0} peaks of the TTB phase are present indicating preferential growth according to the JCPDS file #01-087-1856 of the $\text{K}_6\text{Nb}_{10.88}\text{O}_{30}$ TTB phase (space group: *P4/mbm* (127); $a = 12.5820 \text{ \AA}$, $c = 3.9920 \text{ \AA}$). A minor peak at $2\theta = 14.54^\circ$ indicates the presence of the $\text{K}_4\text{Nb}_6\text{O}_{17}$ phase (JCPDS file #01-076-0977) as a secondary phase. The corresponding SEM micrograph shows long (several microns) and thin crystallites (50 nm wide). Some other crystallites exhibit out-of-plane short nanorod shape (white contrast on the SEM micrograph). The $(\text{K}_{0.58}\text{Na}_{0.42})_{0.62}\text{NbO}_x$ composition is therefore close to the expected one. Morphology of the F2 (perovskite phase) and F3 (TTB phase) films being very similar, further transmission electron microscopy and electron diffraction experiments were performed to get in-plane information.

Figure 4 presents bright field micrographs and electron diffraction patterns (EDP) along the normal of F1, F2 and F3 films. EDP of the $(\text{K}_{0.4}\text{Na}_{0.6})_{0.92}\text{NbO}_3$ perovskite phase (film F1) displays a primitive rectangular cell, which corresponds to the [101] zone axis of a pseudo-cubic cell with lattice parameters close to 4 Å (Figure 4b), as expected from the simulated EDP (Figure 4c). For the purpose of comparison, the (110) SrTiO₃ cell was drawn in red in all the EDPs of Figure 4. The perovskite phase presents therefore epitaxial relationships with the (110) SrTiO₃ substrate, whose cell has roughly the same dimensions. The related relationships are: $[101]_{\text{KNN}} // [101]_{\text{STO}}$, $(010)_{\text{KNN}} // (100)_{\text{STO}}$, $(10\bar{1})_{\text{KNN}} // (10\bar{1})_{\text{STO}}$. Comparison between image and diffraction pattern enable to determine the elongation direction of the small rectangular crystals that form the film, namely the [010] direction. This corresponds to the elongation direction of the distorted octahedral, as drawn in Figure 4d.

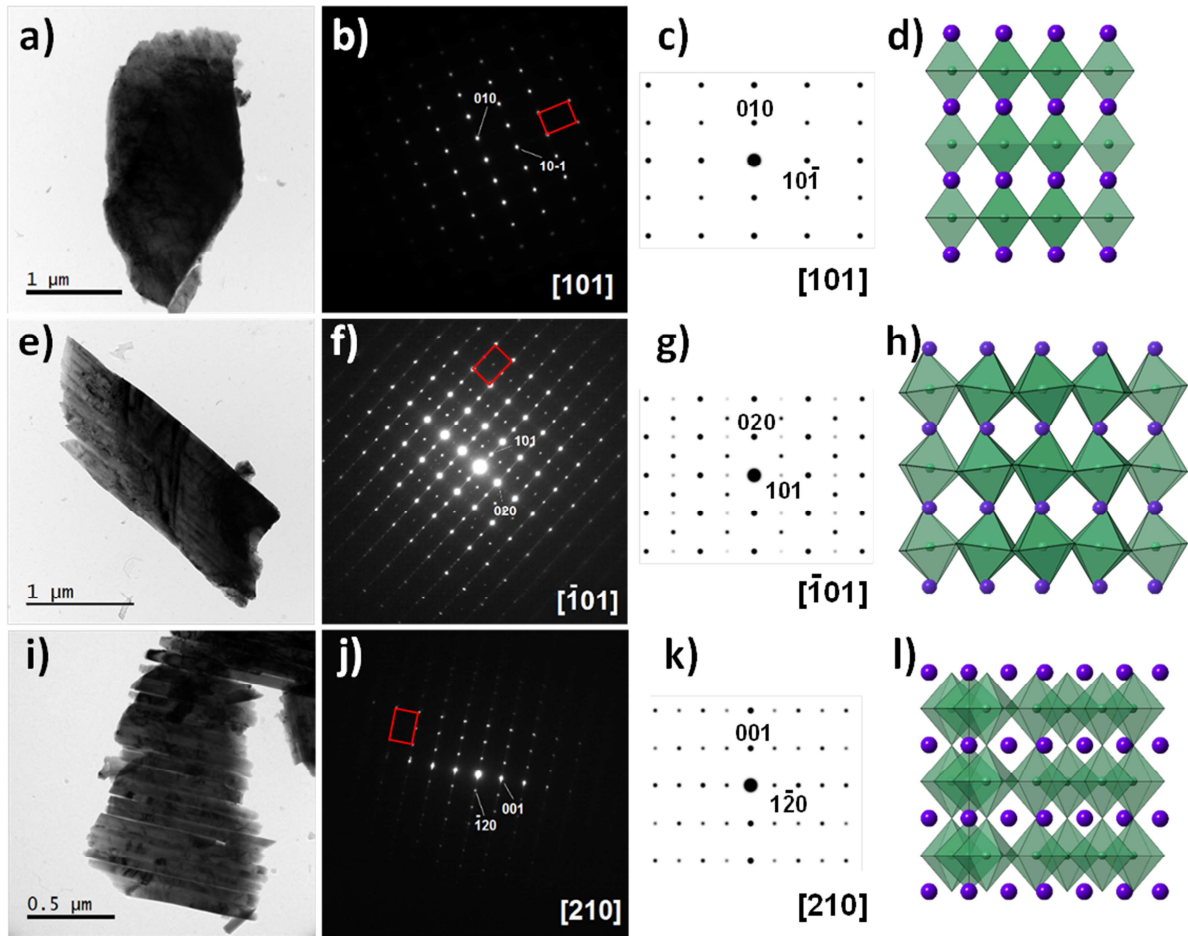


Figure 4. Bright field TEM micrographs, experimental and theoretical electron diffraction patterns and corresponding schemes of the KNN structures under consideration of perovskite F1 film (a,b,c,d), perovskite F2 film (e,f,g,h) and TTB F3 film (i,j,k,l). Red rectangle: scheme of the SrTiO₃ cell.

The EDP of the $K_{0.14}Na_{0.86}NbO_x$ phase (film F2), displayed in Figure 4f, shows a rectangular cell corresponding to a pseudo-cubic phase with lattice parameters twice the ones of a simple perovskite cell (simulated in Figure 4g). Similarly to the previous perovskite phase, the epitaxial relationships are: $[\bar{1}01]_{KNN} // [101]_{STO}$, $(100)_{KNN} // (100)_{STO}$, $(101)_{KNN} // (10\bar{1})_{STO}$. Comparison between the image of the long crystals (Figure 4c) and EDP indicates a [010] elongation direction. This corresponds to the elongation direction of the octahedra in the phase as well (Figure 4h).

EDP of the TTB phase (film F3) along the [210] zone axis is displayed in Figure 4j. As expected, the pattern consists of a primitive rectangular along the above direction (simulation in Figure 4k). Comparison with the substrate cell (red rectangle in Figure 4j) provides the following epitaxial relationships: $[210]_{\text{TTB}}//[101]_{\text{STO}}$, $(001)_{\text{TTB}}//(100)_{\text{STO}}$, $(\bar{1}20)_{\text{TTB}}//(10\bar{1})_{\text{STO}}$. The parallelepiped-shape long crystal elongation is along the [001] direction, as commonly observed for TTB phases [16, 36]. As for the two previous phases, this direction corresponds to a slight distortion of the octahedra. These results agree with the most intense peaks of the TTB film on the XRD pattern (Figure 3a) which correspond to the (210), (420) and (630) reflections. From the XRD ($hk0$) peak position, the lattice parameter a was computed ($a = 12.483 \pm 0.005 \text{ \AA}$), and from the EDP, the lattice parameter c is about $3.99 \pm 0.05 \text{ \AA}$. Along the two in-plane directions, the substrate-film cells mismatches are respectively $\delta_1 = [d(100)_{\text{STO}} - d(001)_{\text{TTB}}]/d(100)_{\text{STO}} = -2.17 \%$ and $\delta_2 = [d(101)_{\text{STO}} - d(120)_{\text{TTB}}]/d(101)_{\text{STO}} = -1.09 \%$.

To enhance the stabilization of the KNN TTB phase thin films by decreasing the alkaline content, films (F4 to F9) were then deposited at temperature $T = 650^\circ\text{C}$ by using a PLD target sintered by SPS with the $(\text{K}_{0.49}\text{Na}_{0.51})_{0.54}\text{NbO}_x$ composition (target T3).

Samples were also grown with various target-substrate distances on C-plane sapphire substrate, *i.e.* $D = 65 \text{ mm}$ (film F7), $D = 60 \text{ mm}$ (film F8), 55 mm (film F9) and 50 mm (not shown). For F7 and F8 films, similar XRD patterns and surface morphologies were observed (see Figure 5 and Figure 6 and related discussion hereafter). For F9 film however, a slight amount of the KNb_3O_8 phase is noticed on XRD pattern. Independently of the substrate type, a target-substrate distance under 60 mm has resulted in the formation of secondary phases. In the following work this distance has been selected to be equal at least to 60 mm .

In order to control the orientation two films were deposited on SrTiO₃ substrates, F4 on (110)SrTiO₃ and F5 on (001)SrTiO₃. In both cases, pure TTB coatings were obtained. XRD pattern of the film F4 presents pure {*hk*0} TTB phase peaks with a strong (210) preferential orientation (Figure 5), in agreement with XRD and TEM observations performed on F3. Nonetheless, SEM micrograph F4 shows crystallites with parallelepiped-shape and shorter than for film F3 (about 50 nm wide and up to 700 nm long, Figure 6a). It could be noted that SEM images of the films synthesized from the T3 target do not exhibit any additional outgrowths or droplets that can often be observed, especially with targets of the KNN system phases which are difficult to densify by conventional synthesis.

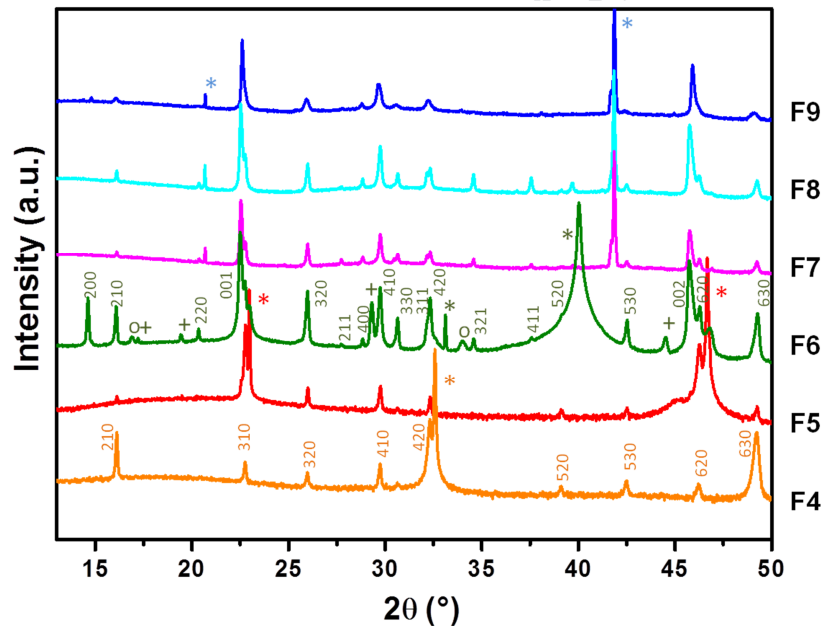


Figure 5. XRD patterns of TTB films grown on (110)STO (film F4, D = 65 mm), (001)STO (film F5, D = 65 mm), (111)Pt/TiO₂/SiO₂/(001)Si (film F6, D = 60 mm) and C-plane sapphire (film F7, D = 65 mm), (film F8, D = 60 mm), (film F9, D = 55 mm) (*: substrates; o: KNb₃O₈; + K₃Nb₇O₁₉) (logarithmic scale).

Regardless of the SrTiO₃ substrate orientation, nanorods present a quite perfect in-plane orientation with almost no vertical nanorods growing along the *c*-axis parallel to the normal of the substrate. On (110) SrTiO₃, the nanorods present a (210) out-of-plane main orientation

and are all growing parallel to each other along the same in-plane direction (film F4, Figure 6a), in line with a lowering of the mismatch between film and substrate cells along this direction (see discussion on the epitaxial relationships for F3). On the (001) SrTiO₃ substrate (film F5, figure 6b), the nanorods are growing along two in-plane directions with a 90° angle to each other (Figure 6b) with a (310) out-of-plane preferential orientation. Corresponding EDP registered along the [310] zone axis (Figure 7b) shows a pseudo-cubic array of reflections. The (001)SrTiO₃ substrate involves this particular orientation due to the small mismatch between the cubic (100) × (010) cell of SrTiO₃ with $d_{100} \times d_{010} = 3.905 \text{ \AA} \times 3.905 \text{ \AA}$ dimensions and the pseudo-cubic cell (001) × (1 $\bar{3}$ 0) of the TTB phase with $d_{001} \times d_{310} = 3.99 \text{ \AA} \times 3.937 \text{ \AA}$ dimensions. These experimental values were determined from the XRD (310) peak position and from the EDP (001) reflection of the individual nanorods registered in microdiffraction conditions (Figures 7d and 7f), respectively. Mismatches between the substrate and the film cells are respectively $\delta_1 = [d(100)_{\text{STO}} - d(001)_{\text{TTB}}] / d(100)_{\text{STO}} = -2.17 \%$ and $\delta_2 = [d(010)_{\text{STO}} - d(130)_{\text{TTB}}] / d(010)_{\text{STO}} = -0.84 \%$. Note that, in contrast to (110)SrTiO₃ substrate, the square cell of the (001)SrTiO₃ plane leads to equivalent mismatches at 90° from each other, explaining the growth of the KNN TTB nanorods along two in-plane orientations as observed in Figure 6b. The corresponding lattice parameters were computed as $a = 12.453 \pm 0.005 \text{ \AA}$ (XRD) and $c = 3.99 \pm 0.05 \text{ \AA}$ (EDP).

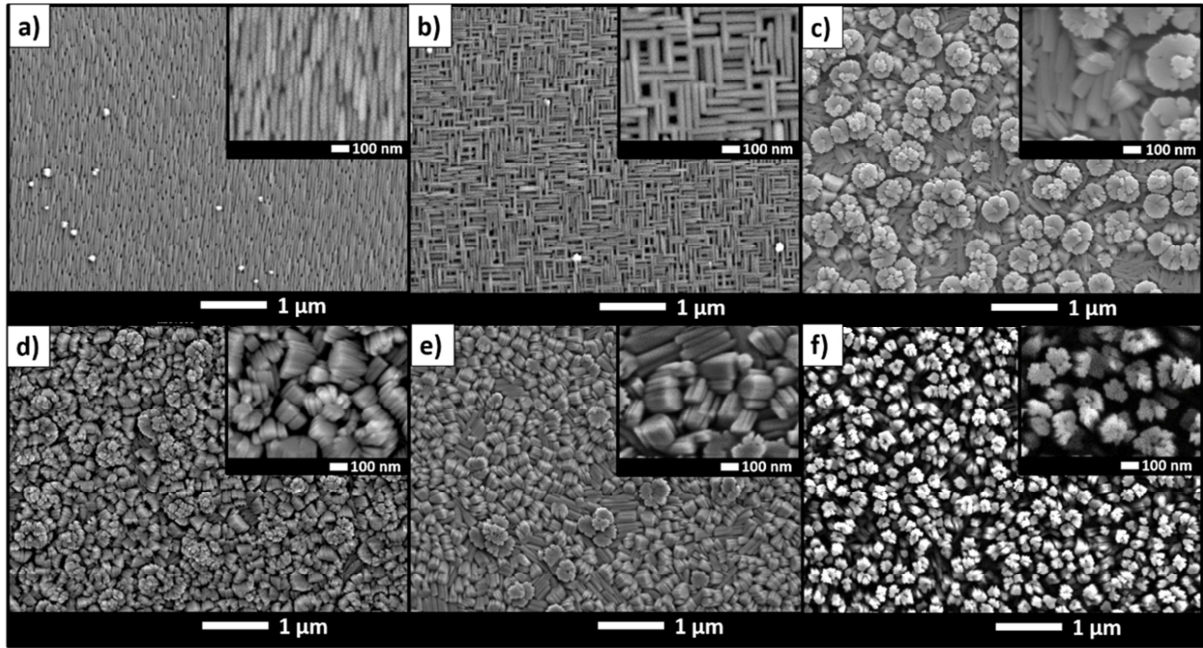


Figure 6. Scanning electron micrographs of the TTB films grown on: (a) (110)STO (film F4, D = 65 mm); (b) (001)STO (film F5, D = 65 mm); (c) (111)Pt/TiO₂/SiO₂/(001)Si (film F6, D = 60 mm); (d) C-plane sapphire (film F7, D = 65 mm); (e) C-plane sapphire (film F8, D = 60 mm), (f) C-plane sapphire (film F9, D = 55 mm).

In addition, microdiffraction pattern of the individual nanorods shows diffuse scattering lines along the $[1\bar{3}0]$ growth direction, indicating some planar disorder perpendicularly to this direction. By dark field method in 2-beams conditions, it was also possible to enlighten individual nanorods along the two different in-plane directions by selecting corresponding diffraction reflections (Figure 7c and 7e).

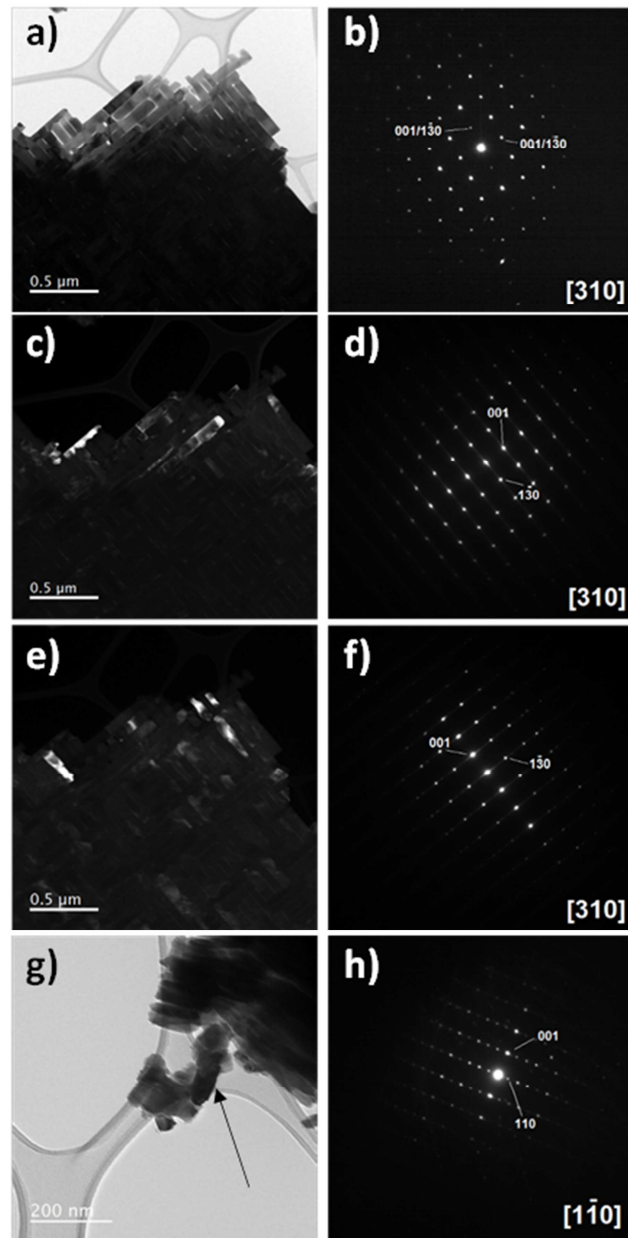


Figure 7. (a) Bright field TEM micrograph of the TTB films grown on (001)STO (film F5); (b) corresponding selected area EDP along the [310] zone axis; (c,e) Dark field TEM micrographs showing individual nanorods growing along the two in-plane directions; (d,f) Microdiffraction EDP of each nanorod variant along the [310] zone axis; (g,h) Bright field TEM micrograph and EDP along the $[1\bar{1}0]$ zone axis of the TTB film grown on C-plane sapphire (film F7). The arrow displays the crystallite corresponding to the EDP.

Thin films were also deposited on Pt and sapphire substrates to perform dielectric characterizations (at low frequency and at microwaves, respectively). XRD pattern of the thin film grown on (111)Pt/TiO₂/SiO₂/(001)Si (film F6) indicates a polycrystalline growth (*i.e.*

random orientation) with a (001) preferential orientation of the nanorods (Figure 5). In that case, the nanorods have grown as thin rod aggregates attached together by their longer edge, as observed on SEM micrograph (Figure 6c). The (001) preferential orientation is consistent with the presence of vertical agglomerated nanorods forming a flower-like microstructure. XRD pattern also exhibits minor secondary phases identified as KNb_3O_8 and $\text{K}_3\text{Nb}_7\text{O}_{19}$ (JCPDS files # 01-075-2182 and #00-084-0812, respectively). The presence of secondary phases in films grown on Pt coated silicon, in contrast to those grown on SrTiO_3 , could be explained by its higher thermal conductivity that increases the substrate surface temperature for the same deposition temperature. It is assumed that these phases presence has a minor impact on the thin film properties due to their small amount (Figure 5).

On C-plane sapphire, XRD patterns on F7 and F8 films show pure TTB phase (Figure 5). For both samples, those patterns exhibit a similar (001/310) preferential growth. TEM experiments performed on the F7 film confirm the elongation direction of nanorods along [001] direction (Figure 7g and 7h). EDXS analyses indicate a lower alkaline elements amount in the TTB nanorods compared with those grown on SrTiO_3 (Table 2). However on both substrates, the films present a sodium/potassium ratio close to 1 and an alkaline elements/niobium ratio slightly lower than the nominal composition $(\text{K,Na})_{0.6}\text{Nb}_{1.1}\text{NbO}_3$, indicating that some cationic sites are therefore partially filled.

3.2. Investigation of the structural characteristics by Raman spectroscopy

Figure 8 shows Raman spectra of the TTB thin film grown on (111)Pt/TiO₂/SiO₂/(001)Si substrate (film F6). At room temperature, the spectra present typical signature of TTB phases compared with that reported for isostructural system [37–41], in agreement with X-ray diffraction and TEM analyses. Modes at 670 cm⁻¹ and 731 cm⁻¹ are assigned to the Nb–O stretching vibrations in the [NbO₆] octahedra, and modes located in the 70 to 400 cm⁻¹ range

is attributed to the O–Nb–O bending modes between adjacent $[\text{NbO}_6]$ octahedra, as observed on other TTB niobates. The broad peaks with important contribution overlap, especially at low frequency region ($< 400 \text{ cm}^{-1}$), are characteristic of the TTB structure with cationic disorder in A1, A2 and C sites. These effects make the assignment of Raman lines hardly attainable, and so, it is impossible to distinguish unambiguously a centrosymmetrical structure from a non-centrosymmetrical one. Temperature-dependent spectra show neither significant shift nor anomaly in peak position and splitting or number modes change between 77 K and 873 K. This result strongly suggests a stable film structure and no clear evidence of any structural transition occurs over the entire temperature range studied.

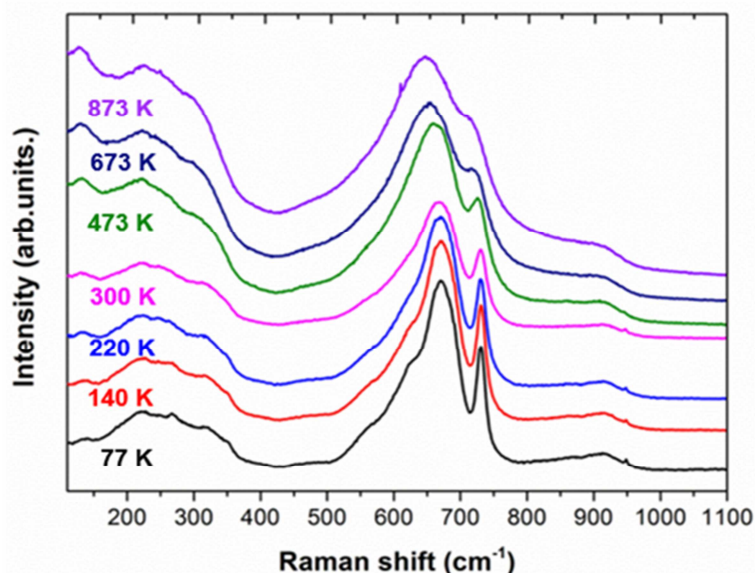


Figure 8. Raman spectra of the TTB thin film deposited on $(111)\text{Pt}/\text{TiO}_2/\text{SiO}_2/(001)\text{Si}$ (film F6) at various temperatures (from 77 K to 873 K)

3.3. Investigation by Piezoelectric Force Microscopy

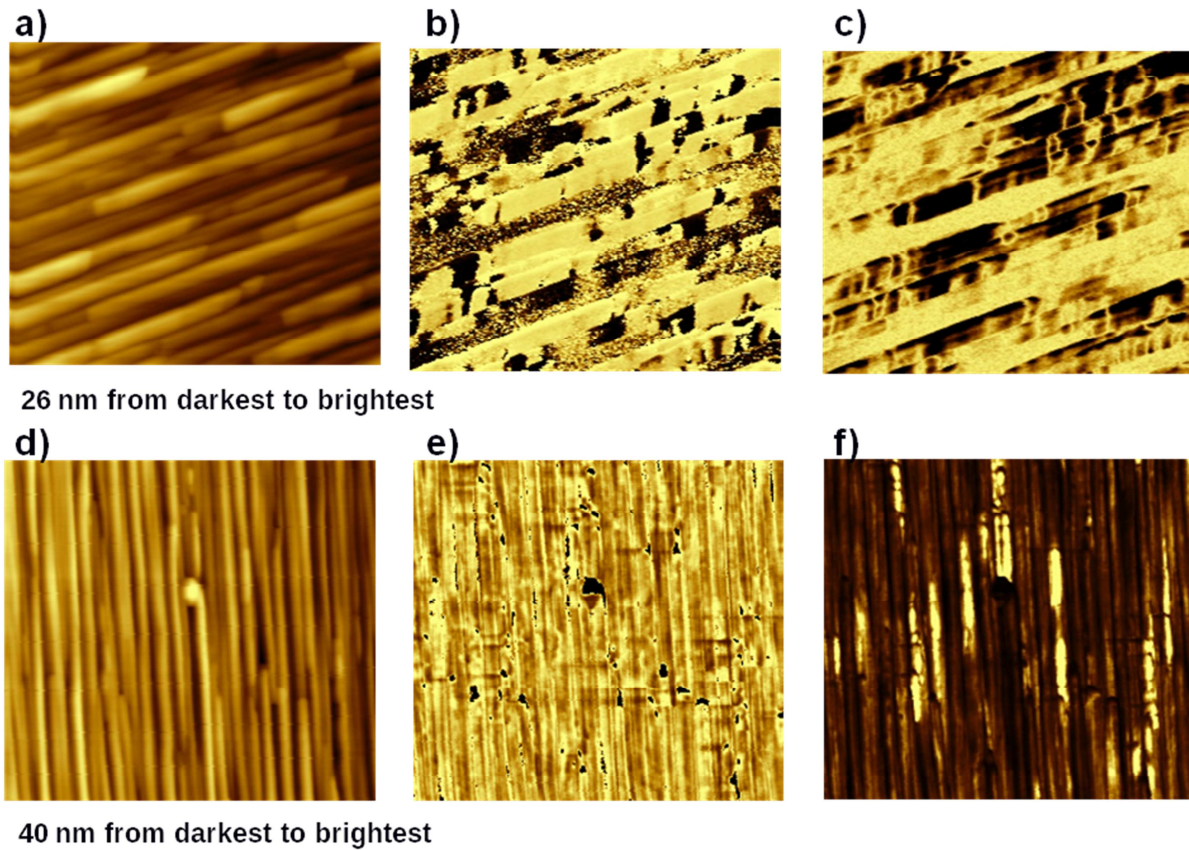


Figure 9. PFM of perovskite (F2) and TTB (F3) films: (a,d) topography; (b,e) phase; (c,f) amplitude. $2\ \mu\text{m} \times 2\ \mu\text{m}$ size images

Piezoelectric Force Microscopy performed in topography mode on F2 and F3 films shows the typical morphologies of the perovskite and TTB-type KNN phases grown on $(110)\text{SrTiO}_3$ (Figure 9a and 9d). In piezoresponse mode (Figure 9b, 9c, 9e and 9f), a clear contrast is observed in both cases, with a heterogeneous piezoelectric response: some grains show a strongest response (bright areas in Figure 9c and 9f) compared with others, with quasi-null amplitude response (dark areas in Figure 9c and 9f). In the case of the perovskite phase (Figure 9a-9c), where the PFM phase signal presents opposite directions of vertical polarization (the histogram of phase values (not shown) is composed of two peaks separated by 180°), this can be explained by a polarization direction in the orthorhombic cell with various directions relatively to the preferential orientation. Indeed the polarization in this kind of perovskite is aligned along the diagonal of the facets of the pseudo-cubic cell, *i.e.* the

$\langle 110 \rangle$ directions. In the present case, these directions correspond either to the normal direction or to the in-plane direction. Concerning the TTB phase, it is expected that the polarization direction is parallel to the [001] direction, therefore to the nanorod growth direction. Whereas a piezoresponse was observed, it has not been possible to reverse the signal by applying a reversed DC bias voltage. This experimental result is assigned to high leakage currents that make impossible to reach the coercive electric field without destroying the sample by Joule effect. In the case of the TTB phase whose properties are not fully established, another possibility concerns the piezoelectric response without ferroelectricity of the sample, at least at room temperature.

3.4. Dielectric characteristics

3.4.1. Low frequency measurements

The dielectric characteristics (ϵ_r and $\tan\delta$) at low frequencies were retrieved from the KNN TTB thin film (F6) grown on (111)Pt/TiO₂/SiO₂/(001)Si substrate. No frequency dispersion of the dielectric characteristics was observed from 1 kHz to 1 MHz with a permittivity value $\epsilon_r \approx 200$ and $\tan\delta \approx 1.5\%$ (Figure 10). The recorded permittivity values are in the same range as to those of other TTB thin films, for instance $\epsilon_r \approx 400$ for K₃Li₂Nb₅O₁₅ epitaxial films [42] and ~ 150 for Ba₂LnFeNb₄O₁₅ (Ln = La, Nd, Eu) polycrystalline films [43], or to other values that can be found for ferroelectric thin films or dielectric relaxors as in the Bi-Zn-Nb-O system [44]. It has to be pointed out that polarization versus electric field measurements have been attempted. However, the high leakage currents make difficult the measurements under DC electric field and it was not possible to observe hysteric loop with saturation of the polarization.

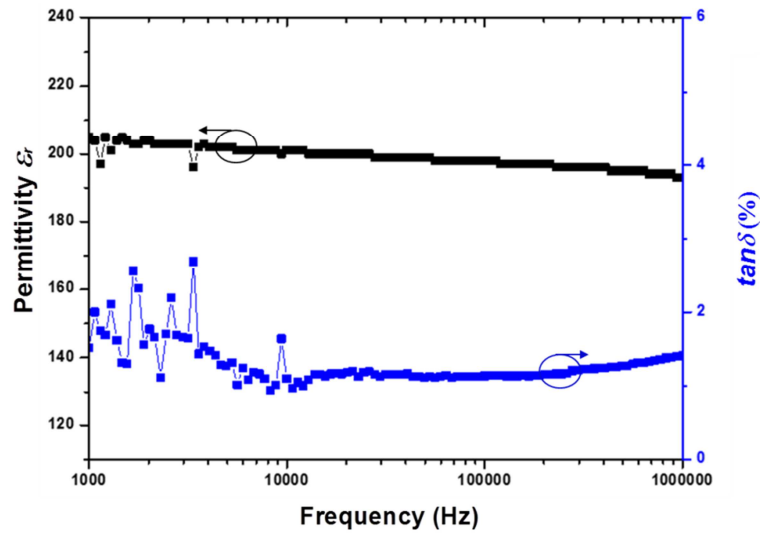


Figure 10. Variation of the dielectric characteristics (permittivity ϵ_r and loss $\tan\delta$) at low frequencies of the TTB thin film (F6) deposited on (111)Pt/TiO₂/SiO₂/(001)Si.

3.4.2. High frequency measurements

The dielectric characteristics (ϵ_r and $\tan\delta$) at high frequencies were retrieved from the KNN TTB thin film (F8) grown on C-plane sapphire substrate. The values were obtained using the measured reflection (S_{11}) and transmission (S_{21}) coefficients of the transmission lines. TTB thin film exhibits a permittivity $\epsilon_r = 135$ at 10 GHz, 130 at 20 GHz, and 125 at 30 GHz showing a good stability versus frequency (Figure 11a). Even though the literature does not present many microwave dielectric characterizations of the TTB phases, permittivity values close to 130 have also been reported for other materials [45, 46]. Nevertheless, these values remain lower than those retrieved from the $K_xNa_{1-x}NbO_3$ perovskite phase in the same settings [47]. The dielectric permittivity decrease of the TTB phase from $\epsilon_r \approx 200$ at low frequency to $\epsilon_r \approx 130$ at high frequency is consistent with the decrease as reported in the literature. The loss tangent value $\tan\delta$ at 10 GHz is about 20 % (Figure 11). The variation of $\tan\delta$ from 1 to 5 GHz is attributed in part of the metal skin depth loss. $\tan\delta$ at high frequencies remains much higher than 1.5 % measured at low frequency. The polyoriented growth of the TTB phase,

especially both in-plane and out-of-plane ordering of the nanorods, led to a quite rough film, and consequently to a rough metal-oxide film interface which may impact the loss.

The dielectric characteristics (ϵ_r and $\tan\delta$) at 10 GHz have shown no significant temperature dependence from 20°C to 240°C (Figure 11b). The variation of the permittivity and the slight increase in $\tan\delta$ from 20% to 23% are attributed to the temperature increase of the device as a whole and of the measurement system. Therefore, the variations are not significant enough to hint a phase transition and are in agreement with the previous observations by Raman spectroscopy. The results also indicate a good stability of the dielectric characteristics at microwave frequencies in this range of temperature.

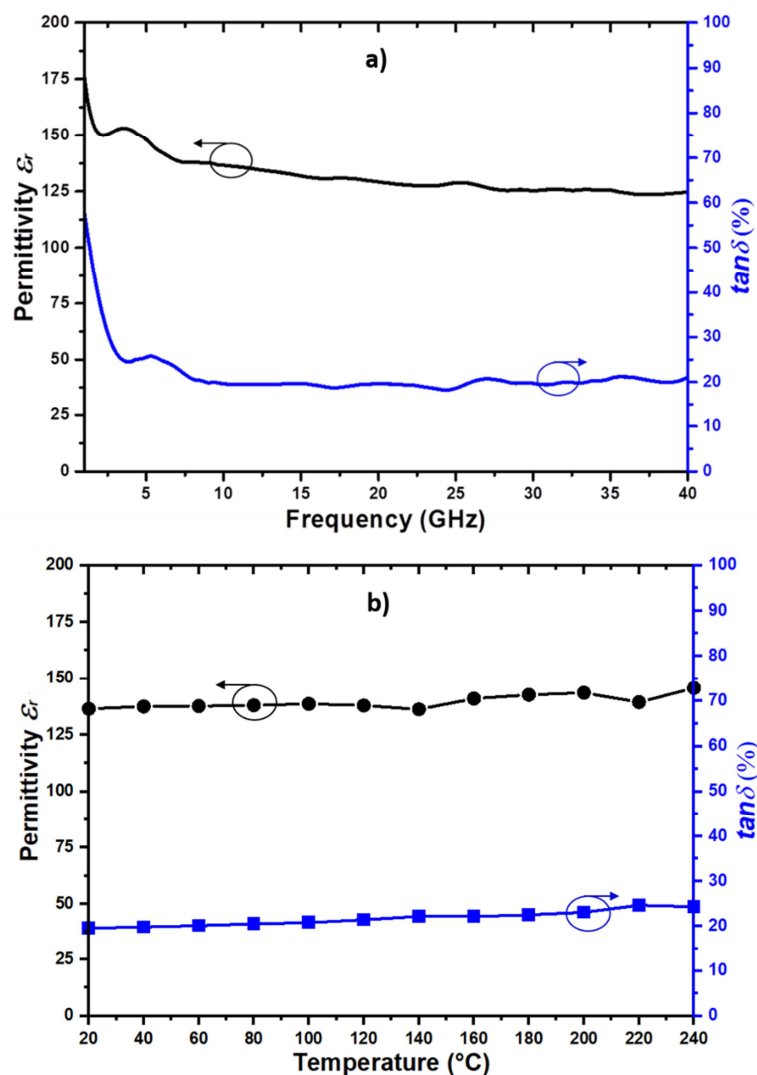


Figure 11. Variation of the dielectric characteristics (permittivity ϵ_r and loss $\tan\delta$) at high frequencies of the TTB thin film (F8) deposited on C-cut sapphire (a) depending on the frequency at room temperature and (b) depending on the temperature at 10 GHz.

The dielectric characteristics were also retrieved from the transmission lines under biasing (E_{bias} up to 27 kV/cm). No significant change was observed. Moreover the resonance frequency F_r of the CPW stub resonator printed on the KNN thin film was measured under various biasing to investigate a possible tunability (not shown here). A slightly open cycle shape has been evidenced, which could suggest a ferroelectric-like behavior. However the weak variation leading to a frequency tunability value lower than 1% could not be considered as a proof of a ferroelectric behavior.

CONCLUSION

A tetragonal tungsten bronze structure in the K-Na-Nb-O system was successfully synthesized in thin films on various substrates using pulsed laser deposition technique. Thin films were deposited on both (100) and (110)SrTiO₃ with a highly oriented growth. Indeed dense microstructures with characteristic in-plane oriented nanorods were evidenced. Complementary characterizations (*i.e.* X-ray and electron diffraction, Raman spectroscopy) have also evidenced the TTB type phase growth. Piezoelectric Force Microscopy has shown an unambiguous piezoelectric local activity. However, high leakage currents made them impossible to switch the TTB polarization under an external DC electric field without destroying the sample.

Dielectric characteristics at room temperature were retrieved at low and high frequencies with a dielectric permittivity $\epsilon_r \approx 200$ at 1 kHz and 130 at 10 GHz from thin films grown on (111)Pt/TiO₂/SiO₂/(001)Si and C-plane sapphire substrates, respectively. The

electrical measurements, that were also restricted by high leakage current, have not shown ferroelectricity.

In order to perform further investigations on the physical behavior, it is essential to suppress the leakage current. For this purpose and to decrease loss, chemical doping could be envisaged as it has been performed in $K_xNa_{1-x}NbO_3$ perovskite phase [48]. Indeed, the vacant crystallographic sites which characterize the TTB structure give a large possibility of improvement, modification and control of the TTB properties.

ACKNOWLEDGEMENTS

The authors warmly thank Dr. S. Quémeré and Dr. P. Lemoine for their help in SPS experiments, C. Derouet for technical assistance for X-Ray diffraction, and S. Ollivier for her assistance in thin films preparation and characterization (ISCR) and P. Hamoumou for his assistance for PFM measurements (INL).

The scanning electron microscopy and transmission electron microscopy were performed in ScanMAT UMS 20001 CNRS-University of Rennes 1.

The authors are grateful for the financial support of the Direction Générale de l'Armement (DGA) and the Région Bretagne (PhD research Grant of B. Aspe, project ARMin). ISCR and ScanMAT received a financial support from the Région Bretagne, Rennes Métropole, the Département d'Ille et Vilaine and the European Union (CPER-FEDER 2007–2014, Présage Nos. 39126 and 37339, and CPER SCANMAT 2015-2020 MULTIMAT ScanMAT). This work was also supported by the European Union through the European Regional Development Fund (ERDF), the Ministry of Higher Education and Research, the Région Bretagne, the Département des Côtes d'Armor and Saint-Brieuc Armor Agglomération,

through the CPER Projects 2015-2020 MULTIMAT MATECOM and SOPHIE / STIC & Ondes.

REFERENCES

1. D.L. Polla, Microelectromechanical systems based on ferroelectric thin films. *Microelectron Eng* 29:51–58 (1995). [https://doi.org/10.1016/0167-9317\(95\)00114-X](https://doi.org/10.1016/0167-9317(95)00114-X)
2. N. Setter, D. Damjanovic, L. Eng, G. Fox, S. Gevorgian, S. Hong, A. Kingon, H. Kohlstedt, N.Y. Park, G.B. Stephenson, I. Stolitchnov, A.K. TagansteV, D.V. Taylor, T. Yamada, S. Steiffer, Ferroelectric thin films: Review of materials, properties, and applications. *J Appl Phys* 100:051606 (2006). <https://doi.org/10.1063/1.2336999>
3. A. Petosa, An Overview of Tuning Techniques for Frequency-Agile Antennas. *IEEE Antennas Propag Mag* 54:271–296 (2012). <https://doi.org/10.1109/MAP.2012.6348178>
4. V. Ishchuk, D. Kuzenko, V. Sobolev, Piezoelectric and functional properties of materials with coexisting ferroelectric and antiferroelectric phases. *AIMS Mater Sci* 5:711–741 (2018). <https://doi.org/10.3934/matensci.2018.4.711>
5. Y. Saito, H. Takao, T. Tani, T. Nonoyama, K. Takatori, T. Homma, T. Nagaya, M. Nakamura, Lead-free piezoceramics. *Nature* 432:84–87 (2004). <https://doi.org/10.1038/nature03028>
6. J.-F. Li, K. Wang, F.-Y. Zhu, L.-Q. Cheng, F.-Z. Yao, (K,Na)NbO₃-Based Lead-Free Piezoceramics: Fundamental Aspects, Processing Technologies, and Remaining Challenges. *J Am Ceram Soc* 96:3677–3696 (2013). <https://doi.org/10.1111/jace.12715>
7. J. Wu, D. Xiao, J. Zhu, Potassium–Sodium Niobate Lead-Free Piezoelectric Materials: Past, Present, and Future of Phase Boundaries. *Chem Rev* 115:2559–2595 (2015). <https://doi.org/10.1021/cr5006809>
8. M.R. Bafandeh, R. Gharakhani, J.-S. Lee, Dielectric and piezoelectric properties of sodium potassium niobate-based ceramics sintered in microwave furnace. *Mater Chem Phys* 156:254–260 (2015). <https://doi.org/10.1016/j.matchemphys.2015.03.018>
9. M. Peddigari, V. Patel, G.P. Bharti, A. Khare, D. Pamu, Microwave dielectric and nonlinear optical studies on radio-frequency sputtered Dy₂O₃-doped KNN thin films. *J Am Ceram Soc* 100:3013–3023 (2017). <https://doi.org/10.1111/jace.14846>
10. F. Fan, X. Zhao, F. Wang, Q. Yue, H. Zhou, H. Luo, Y. Tang, Z. Duan, W. Shi, B. Fang, Design and fabrication of high frequency ultrasonic transducer based on lead-free Mn-doped (K_{0.44}Na_{0.56})NbO₃ single crystal. *Sens Actuators Phys* 267:182–186 (2017). <https://doi.org/10.1016/j.sna.2017.10.018>
11. Y. Sun, F. Guo, Q. Lu, S. Zhao, Improved ferroelectric photovoltaic effect in Mn-doped lead-free K_{0.5}Na_{0.5}NbO₃ films. *Ceram Int* 44:13994–13998 (2018). <https://doi.org/10.1016/j.ceramint.2018.04.250>

12. J.-C. Grivel, K. Thydén, J.R. Bowen, A.B. Haugen, Deposition of highly oriented (K,Na)NbO₃ films on flexible metal substrates. *Thin Solid Films* 650:7–10 (2018). <https://doi.org/10.1016/j.tsf.2018.02.008>
13. J. Du, Z. Xu, R. Chu, J. Hao, W. Li, G. Jiang, P. Zheng, Rare-earth doped (K_{0.5}Na_{0.5})NbO₃ multifunctional ceramics. *J Mater Sci Mater Electron* 28:5288–5294 (2017). <https://doi.org/10.1007/s10854-016-6186-6>
14. R. Castañeda-Guzmán, R. López-Juárez, J.J. Gervacio, M.P. Cruz, S. Díaz de la Torre, S.J. Pérez-Ruiz, Structural and piezo-ferroelectric properties of K_{0.5}Na_{0.5}NbO₃ thin films grown by pulsed laser deposition and tested as sensors. *Thin Solid Films* 636:458–463 (2017). <https://doi.org/10.1016/j.tsf.2017.06.039>
15. S. Garroni, N. Senes, A. Iacomini, S. Enzo, G. Mulas, L. Pardo, S. Cuesta-Lopez, Advanced Synthesis on Lead-Free K_xNa_(1-x)NbO₃ Piezoceramics for Medical Imaging Applications. *Phys Status Solidi A* 1700896 (2018). <https://doi.org/10.1002/pssa.201700896>
16. Q. Simon, V. Dorcet, P. Boullay, V. Demange, S. Députier, V. Bouquet, M. Guilloux-Viry, Nanorods of Potassium Tantalum Niobate Tetragonal Tungsten Bronze Phase Grown by Pulsed Laser Deposition. *Chem Mater* 25:2793–2802 (2013). <https://doi.org/10.1021/cm401018k>
17. B.A. Scott, E.A. Giess, B.L. Olson, G. Burns, A.W. Smith, D.F. O'Kane, The tungsten bronze field in the system K₂O|Li₂O|Nb₂O₅. *Mater Res Bull* 5:47–56 (1970). [https://doi.org/10.1016/0025-5408\(70\)90072-3](https://doi.org/10.1016/0025-5408(70)90072-3)
18. A.A. Awadalla, B.M. Gatehouse, Crystal structures of some niobium and tantalum oxides. III K₆Ta_{10.8}O₃₀ - A partially “Filled” tetragonal tungsten bronze-like structure. *J Solid State Chem* 23:349–355 (1978). [https://doi.org/10.1016/0022-4596\(78\)90083-X](https://doi.org/10.1016/0022-4596(78)90083-X)
19. M. Lundberg, M. Sundberg, Studies of phases in the KNbO₃-Nb₂O₅ system by high-resolution electron microscopy and X-ray powder diffraction. *J Solid State Chem* 63:216–230 (1986). [https://doi.org/10.1016/0022-4596\(86\)90172-6](https://doi.org/10.1016/0022-4596(86)90172-6)
20. F. Madaro, R. Sæterli, J.R. Tolchard, M.-A. Einarsrud, R. Holmestad, T. Grande, Molten salt synthesis of K₄Nb₆O₁₇, K₂Nb₄O₁₁ and KNb₃O₈ crystals with needle- or plate-like morphology. *CrystEngComm* 13:1304–1313 (2011). <https://doi.org/10.1039/C0CE00413H>
21. A. Simon, J. Ravez, Solid-state chemistry and non-linear properties of tetragonal tungsten bronzes materials. *Comptes Rendus Chim* 9:1268–1276 (2006). <https://doi.org/10.1016/j.crci.2006.04.001>
22. R.R. Neurgaonkar, W.K. Cory, J.R. Oliver, L.E. Cross, Growth and properties of tungsten bronze K₃Li₂Nb₅O₁₅ single crystals. *Mater Res Bull* 24:1025–1030 (1989). [https://doi.org/10.1016/0025-5408\(89\)90188-8](https://doi.org/10.1016/0025-5408(89)90188-8)
23. X. Fan, Y. Wang, Y. Jiang, Structure and electrical properties of MnO₂-doped Sr_{2-x}Ca_xNaNb₅O₁₅ lead-free piezoelectric ceramics. *J Alloys Compd* 509:6652–6658 (2011). <https://doi.org/10.1016/j.jallcom.2011.03.130>

24. R.Q. Yin, P. Zheng, J.C. Wang, L.M. Dai, J. Du, L. Zheng, J.X. Deng, K.X. Song, H.B. Qin, Structural and electrical properties of K-doped $\text{Sr}_{1.85}\text{Ca}_{0.15}\text{NaNb}_5\text{O}_{15}$ lead-free piezoelectric ceramics. *Ceram Int* 42:10349–10354 (2016). <https://doi.org/10.1016/j.ceramint.2016.03.159>
25. R.Z. Mehdiyeva, A.I. Mammadov, R.E. Huseynov, S. Kafarova, T. Çoşkun, M.Y. Seyidov, Preparation, structure analysis and dielectric characteristics of the novel ferroelectric ceramics $(1-x)\text{Sr}_{3.35}\text{Ba}_{1.65}\text{Nb}_{10}\text{O}_{30}(\text{SBN})-(x)\text{Ba}_4\text{Na}_2\text{Nb}_{10}\text{O}_{30}(\text{BNN})$ with potassium tungsten-bronze structure. *J Alloys Compd* 711:169–183 (2017). <https://doi.org/10.1016/j.jallcom.2017.03.309>
26. G. Zhu, Z. Ci, C. Ma, Y. Shi, Y. Wang, A novel red emitting phosphor of Eu^{3+} doped TTB-type niobate $\text{NaSr}_2\text{Nb}_5\text{O}_{15}$ for white LEDs. *Mater Res Bull* 48:1995–1998 (2013). <https://doi.org/10.1016/j.materresbull.2012.12.074>
27. A. Kudo, H. Okutomi, H. Kato, Photocatalytic Water Splitting into H_2 and O_2 over $\text{K}_2\text{LnTa}_5\text{O}_{15}$ Powder. *Chem Lett* 29:1212–1213 (2000). <https://doi.org/10.1246/cl.2000.1212>
28. J. Hreščak, B. Malič, J. Cilenšek, A. Benčan, Solid-state synthesis of undoped and Sr-doped $\text{K}_{0.5}\text{Na}_{0.5}\text{NbO}_3$: Study by thermal analysis and in situ high-temperature X-ray diffraction. *J Therm Anal Calorim* 127:129–136 (2017). <https://doi.org/10.1007/s10973-016-5615-3>
29. F. Rubio-Marcos, P. Marchet, T. Merle-Méjean, J.F. Fernandez, Role of sintering time, crystalline phases and symmetry in the piezoelectric properties of lead-free KNN-modified ceramics. *Mater Chem Phys* 123:91–97 (2010). <https://doi.org/10.1016/j.matchemphys.2010.03.065>
30. J. Fuentes, J. Portelles, M.D. Durruthy-Rodríguez, H. H'Mok, O. Raymond, J. Heiras, M.P. Cruz, J.M. Siqueiros, Dielectric and piezoelectric properties of the KNN ceramic compound doped with Li, La and Ta. *Appl Phys A* 118:709–715 (2015). <https://doi.org/10.1007/s00339-014-8783-7>
31. A. Waroquet, V. Demange, N. Hakmeh, J. Perrière, S. Freslon, S. Députier, M. Guilloux-Viry, Epitaxial growth and cationic exchange properties of layered KNb_3O_8 thin films. *RSC Adv* 7:15482–15491 (2017). <https://doi.org/10.1039/C7RA00261K>
32. A. Waroquet, Couches-minces dans le système K-Nb-O : croissance épitaxiale et nanostructuration par PLD de phases pérovskite, TTB et lamellaires. Thesis, Rennes 1, (2015).
33. S. Mustofa, T. Araki, T. Furusawa, M. Nishida, T. Hino, The PLD of BaTiO_3 target produced by SPS and its electrical properties for MLCC application. *Mater Sci Eng B* 103:128–134 (2003). [https://doi.org/10.1016/S0921-5107\(03\)00160-0](https://doi.org/10.1016/S0921-5107(03)00160-0)
34. M. Bah, F. Giovannelli, F. Schoenstein, G. Feuillard, E. Le Clezio, I. Monot-Laffez, High electromechanical performance with spark plasma sintering of undoped $\text{K}_{0.5}\text{Na}_{0.5}\text{NbO}_3$ ceramics. *Ceram Int* 40:7473–7480 (2014). <https://doi.org/10.1016/j.ceramint.2013.12.097>

35. Q. Simon, Y. Corredores, X. Castel, R. Benzerga, R. Sauleau, K. Mahdjoubi, A. Le Febvrier, S. Députier, M. Guilloux-Viry, L. Zhang, P. Laurent, G. Tanné, Highly tunable microwave stub resonator on ferroelectric $\text{KTa}_{0.5}\text{Nb}_{0.5}\text{O}_3$ thin film. *Appl Phys Lett* 99:092904 (2011). <https://doi.org/10.1063/1.3626040>
36. F. Brik, R. Enjalbert, C. Roucau, J. Galy, TTB Structure of $\text{K}_4\text{Ce}_2\text{M}_{10}\text{O}_{30}$ (M= Nb or Ta): Crystal Growth and Joint X-Ray and HREM Studies. *J Solid State Chem* 122:7–14 (1996). <https://doi.org/10.1006/jssc.1996.0073>
37. G. Burns, J.D. Axe, D.F. O’Kane, Raman measurements of $\text{NaBa}_2\text{Nb}_5\text{O}_{15}$ and related ferroelectrics. *Solid State Commun* 7:933–936 (1969). [https://doi.org/10.1016/0038-1098\(69\)90545-6](https://doi.org/10.1016/0038-1098(69)90545-6)
38. V. Hornebecq, C. Elissalde, V. Porokhonsky, V. Bovtun, J. Petzelt, M. Maglione, J. Ravez, Dielectric relaxation in tetragonal tungsten bronze ceramics. *J Phys Chem Solids* 64:471–476 (2003). [https://doi.org/10.1016/S0022-3697\(02\)00342-6](https://doi.org/10.1016/S0022-3697(02)00342-6)
39. Y. Amira, Y. Gagou, A. Menny, D. Mezzane, A. Zegzouti, M. Elaatmani, M. El Marssi, Structural and Raman properties of the tetragonal tungsten bronze ferroelectric $\text{Pb}_{2(1-x)}\text{K}_{1+x}\text{Gd}_x\text{Nb}_5\text{O}_{15}$. *Solid State Commun* 150:419–423 (2010). <https://doi.org/10.1016/j.ssc.2009.12.004>
40. A.R.F. Lima, J.C. Sczancoski, M. Siu Li, E. Longo, E.R. Camargo, Structural characterization and photoluminescence behavior of pure and doped potassium strontium niobates ceramics with tetragonal tungsten–bronze structure. *Ceram Int* 42:4709–4714 (2016). <https://doi.org/10.1016/j.ceramint.2015.11.130>
41. Y. Yao, K. Guo, D. Bi, T. Tao, B. Liang, C.L. Mak, S.G. Lu, Pyroelectric properties of calcium doped strontium barium niobate ceramics $\text{Sr}_{0.65-x}\text{Ca}_x\text{Ba}_{0.35}\text{Nb}_2\text{O}_6$ ($x = 0.05$ – 0.425). *J Mater Sci Mater Electron* 29:17777–17785 (2018). <https://doi.org/10.1007/s10854-018-9885-3>
42. B. Allouche, Y. Gagou, A. Belboukhari, F. Le Marrec, M. El Marssi, Structural and electrical properties of $\text{K}_3\text{Li}_2\text{Nb}_5\text{O}_{15}$ thin film grown by pulsed laser deposition. *Mater Res Bull* 94:287–290 (2017). <https://doi.org/10.1016/j.materresbull.2017.06.018>
43. R. Bodeux, D. Michau, M. Josse, M. Maglione, Dielectric properties of tetragonal tungsten bronze films deposited by RF magnetron sputtering. *Solid State Sci* 38:112–118 (2014). <https://doi.org/10.1016/j.solidstatesciences.2014.10.007>
44. A. Le Febvrier, S. Députier, V. Demange, V. Bouquet, A.C. Galca, A. Iuga, L. Pintilie, M. Guilloux-Viry, Effect of in-plane ordering on dielectric properties of highly {111}-oriented bismuth–zinc–niobate thin films. *J Mater Sci* 52:11306–11313 (2017). <https://doi.org/10.1007/s10853-017-1297-x>
45. Z. Xiong, B. Tang, C. Yang, S. Zhang, Correlation between structures and microwave dielectric properties of $\text{Ba}_{3.75}\text{Nd}_{9.5-x}\text{Sm}_x\text{Ti}_{17.5}(\text{Cr}_{1/2}\text{Nb}_{1/2})_{0.5}\text{O}_{54}$ ceramics. *J Alloys Compd* 740:492–499 (2018). <https://doi.org/10.1016/j.jallcom.2017.10.072>
46. K. Fukuda, R. Kitoh, I. Awai, Microwave characteristics of $\text{BaPr}_2\text{Ti}_4\text{O}_{12}$ and $\text{BaPr}_2\text{Ti}_5\text{O}_{14}$ ceramics. *J Mater Res* 10:312–319 (1995). <https://doi.org/10.1557/JMR.1995.0312>

47. B. Aspe, F. Cissé, X. Castel, V. Demange, S. Députier, S. Ollivier, V. Bouquet, L. Joanny, R. Sauleau, M. Guilloux-Viry, $K_xNa_{1-x}NbO_3$ perovskite thin films grown by pulsed laser deposition on R-plane sapphire for tunable microwave devices. *J Mater Sci* 53:13042–13052 (2018). <https://doi.org/10.1007/s10853-018-2593-9>
48. S.Y. Lee, C.W. Ahn, A. Ullah, H.J. Seog, J.S. Kim, S.H. Bae, I.W. Kim, Effect of Mn substitution on ferroelectric and leakage current characteristics of lead-free $(K_{0.5}Na_{0.5})(Mn_xNb_{1-x})O_3$ thin films. *Curr Appl Phys* 11:S266–S269 (2011). <https://doi.org/10.1016/j.cap.2011.03.050>

Journal Pre-proof

Highlights:

- Pure tetragonal tungsten bronze phase films were grown by PLD in the KNN system
- The TTB structural features were shown by transmission electron microscopy and XRD
- Highly oriented thin films were grown on (100) and (110) SrTiO₃ substrates
- Dielectric characteristics were determined at low frequencies and in microwave
- High dielectric permittivity ($\epsilon_r > 120$) was witnessed up to 40 GHz

Journal Pre-proof

Declaration of interests

The authors declare that they have no known competing financial interests or personal relationships that could have appeared to influence the work reported in this paper.

The authors declare the following financial interests/personal relationships which may be considered as potential competing interests:

Journal Pre-proof